Journal of ELECTRONIC MATERIALS, Vol. 48, No. 7, 2019
https://doi.org/10.1007/s11664-019-07231-5

Synthesis, Characterization and Gas Sensing Properties of Ga-Doped SnO_2 Nanostructures

GURPREET SINGH[1] and RAVI CHAND SINGH[2,3]

1.—Department of Applied Physics, Chandigarh University, Gharuan, Mohali, Punjab, India. 2.—Department of Physics, Guru Nanak Dev University, Amritsar 143005, India. 3.—e-mail: ravichand.singh@gmail.com

In this work influence of Ga-doping on the sensor response and selectivity of SnO_2 based sensors has been investigated in detail. The effect of in-plane and bridging oxygen vacancies on the gas sensing properties of SnO_2 has also been investigated. Raman and photoluminescence results revealed that defect concentration increases with increase in Ga concentration. A Brunauer–Emmett–Teller (BET) study disclosed that specific surface area increases with increase in Ga content. It has been observed that Ga-doped SnO_2 nanostructures exhibited temperature dependent selectivity towards acetone and hydrogen. It is found that a 3% Ga-doped SnO_2 based sensor is selective to acetone at 200°C while it is selective to hydrogen at 300°C. The observed temperature dependent selectivity of 3% Ga-doped SnO_2 might be due to its different catalytic properties towards acetone and hydrogen. The increased surface area and abundant in-plane oxygen vacancies of Ga-doped SnO_2 samples provided an enhanced sensor response towards 100 ppm of acetone and hydrogen, respectively. The influence of particle size on the intergranular activation energy has been investigated as well.

Key words: Acetone, hydrogen, oxygen vacancies, surface area, selectivity

INTRODUCTION

Acetone is one of the highly volatile organic compounds which finds extensive applications in laboratories as well as in industries for purification of paraffin, dissolving plastic and pharmaceutics, etc.[1] In addition, acetone can create serious health problems such as skin and eye irritation, vomiting, etc., and its inhalation may lead to damage of kidney, liver and pancreas.[2] Therefore, it is essential to fabricate extremely sensitive and selective acetone sensors for environment safety and healthcare purposes. On the other hand, detection of hydrogen is equally important because it is an odorless, colorless and highly inflammable gas.[3] It is widely used as a clean energy source in industries as well as for commercial applications. It is necessary to fabricate low cost and high performance hydrogen sensors for early detection of hydrogen at the work place. Recently, resistive type metal oxide based gas sensors have been widely used for the detection of reducing and oxidizing gases. SnO_2, a *n*-type wide band gap semiconductor, is considered as a novel material for gas sensing applications due to its low cost, good chemical and thermal stability and high versatility.[4,5] However, pure SnO_2 inherently exhibits several limitations such as high operating temperature, lack of selectivity and low sensitivity. Several strategies such as morphology modulation, surface area enhancement, tuning of oxygen vacancies, heterojunction construction, etc., have been effectively used for enhancing the performance of SnO_2 based gas sensors.[6–9] Currently two popular approaches; increasing surface area and doping, are being used for enhancing the performance of SnO_2 based sensors.[10,11]

(Received September 12, 2018; accepted April 16, 2019; published online April 24, 2019)

It has been reported that when the particle size of SnO_2 approaches 6 nm (equal to twice the thickness of a Debye length) the sensitivity of a sensor increases abruptly. Under such situations, the whole of the crystallite is depleted of electrons and consequently the sensitivity becomes a function of crystallite size.[12] Rothschild et al.[13] reported the effect of grain size on the sensitivity of SnO_2 based sensors and their theoretical simulations revealed that the response of SnO_2 based sensor towards reducing gases is inversely proportional to crystallite size. Kida et al.[14,15] studied the effect of particle and pore size on hydrogen gas sensing properties of SnO_2. They reported that sensor response towards hydrogen gas increases as particle size decreases. Doping is a novel approach which efficiently improves sensitivity, selectivity and optimum operating temperature of SnO_2 based gas sensors towards reducing gases.[16,17] It is found from the literature that doping with metal ions increases specific surface area and produces oxygen vacancies in a SnO_2 lattice.[18] Xu et al.[19] systematically studied the effect of vanadium doping on the hydrogen gas sensing properties of SnO_2 based sensors and found that appropriate amounts of vanadium doping in SnO_2 exhibits good sensitivity and selectivity towards hydrogen. Lin et al.[20] reported the effect of Ni doping on the gas sensing properties of SnO_2 based sensors toward volatile organic compounds. They observed that Ni doping considerably increases the sensor response towards volatile organic compounds which is attributed to the increased surface area and formation of oxygen vacancies in doped SnO_2. Moreover, it is reported that metal doping in metal oxide can lower the optimum operating temperature of sensors owing to the creation of oxygen vacancies in the host lattice.[21] The large surface area and abundant amount of oxygen vacancies facilitate the adsorption of oxygen on the surface of SnO_2 which consequently increases sensor response. Bonu et al.[22] investigated the effect of in-plane and bridging oxygen vacancies on the sensor response of SnO_2 based sensor towards methane. They found that in-plane oxygen vacancies play an important role in detecting the methane at a low temperature. Most of the researchers tried to improve the hydrogen gas sensing properties of SnO_2 by doping it with noble metals.[23,24] However noble metals are expensive and prone to poisoning from sulphur species. In order to overcome the above limitations, we have selected Ga as a dopant, which significantly improved sensitivity and selectivity of SnO_2 towards hydrogen and acetone, because of its excellent catalytic properties.[25] It is well reported in the literature that introduction of Ga into metal oxides greatly improves gas sensing properties.[26] The catalytic properties of Ga reduced the optimum operable temperature of sensors (in the present study) for hydrogen sensing. Furthermore, since ionic radii of Ga^{3+} (0.62 Å) is smaller than that of Sn^{4+} (0.71 Å), as a result Ga^{3+} can easily substitute for Sn^{4+} in the SnO_2 lattice.[27] In this work we report for the first time the temperature dependent selectivity of Ga-doped SnO_2 nanostructures towards acetone and hydrogen. It has been observed that a 3% Ga-doped SnO_2 based sensor is selective to acetone at 200°C where it is selective to hydrogen at 300°C. Moreover, the effect of in-plane and bridging oxygen vacancies on the gas sensing properties of SnO_2 has been investigated in detail as well. It has been observed that Ga-doped SnO_2 samples exhibited enhanced sensor response towards 100 ppm of acetone and hydrogen, which is attributed to increased surface area and augmented concentration of in-plane oxygen vacancies.

EXPERIMENTAL SECTION

Synthesis of Undoped and Ga-Doped SnO_2 Nanoparticles

In this work analytical grade chemicals were utilized for the fabrication of undoped as well as Ga-doped SnO_2 nanoparticles.

Undoped as well as Ga-doped SnO_2 nanostructures were fabricated via the co-precipitation method. In the beginning 0.2 M aqueous solution of $SnCl_4{\cdot}5H_2O$ was prepared to which ammonium hydroxide was dripped until its pH became 9. This process resulted in white precipitates which were centrifuged, washed, dried and finally calcined at 500°C for 3 h. Similarly, Ga-doped SnO_2 nanoparticles with different Ga concentrations were prepared by the addition of a calculated amount of $Ga(NO_3)_3{\cdot}5H_2O$ into $SnCl_4{\cdot}5H_2O$ aqueous solution.

Material Characterization

In the present study various techniques were used for the characterization of synthesized nanoparticles. The structural properties of synthesized nanoparticles have been explored using a Shimadzu 7000 Diffractometer system which uses Cu Kα radiation. The specific surface area of prepared samples was analyzed with the help of a Brunauer–Emmett–Teller (BET) surface area analyzer Micromeritics ASAP 2020. Field emission scanning electron microscopy (FESEM) images of samples have been recorded using Carl Zeiss SUPRA 55. The morphology of prepared samples has been investigated by recording their transmission electron microscope (TEM) images with a JEOL JEM-2100 working at 200 kV. X-ray photo electron spectroscopy (XPS) spectra of nanoparticles have been acquired from a Thermo Scientific K-Alpha XPS system with an Al-K_α monochromatic x-ray source. Raman spectra of nanoparticles were obtained from a Renishaw InVia Reflex Micro Raman spectrometer at an excitation wavelength of 514 nm. Photoluminescence spectra (PL) of all the samples have been acquired from a Perkin Elmer LS55 fluorescence spectrometer.

Thick Film Fabrication and Sensor Response Measurement

The following procedure has been implemented for the fabrication of thick film sensors.

At first a suitable amount of SnO_2 powder sample was thoroughly mixed with a few drops of distilled water to obtain a paste. The paste was coated over alumina substrate to get a thick film (thickness $\sim$ 30 μm) between two pre-deposited gold electrodes. The thick film sensor was cured at 300°C for 1 h. By adopting the above procedure, Ga-doped SnO_2 sensors were fabricated for the testing of target gases. To obtain sensors of identical geometry, all the alumina substrates were appropriately masked using polymer film and, after painting with sensing material, extra wet material got removed. The gold electrode on the alumina substrate was deposited using liquid bright gold (Hobby Colorobbia Bright Gold paste). The gas sensing properties of fabricated sensors was studied by home assembled apparatus. The detailed explanation of the measurement system has been reported elsewhere.[28] The variation of real time voltage signal across resistance R_L connected in series (Fig. 1) with a sensor has been measured with a data acquisition system and computer.

The sensor response of fabricated sensors has been determined using the following formula:

$$S = R_a/R_g, \quad (1)$$

where R_a is the sensor resistance in air ambience whereas R_g is resistance in the presence of a air/gas mixture, respectively.

The current (I) flowing through the circuit has been calculated using the relation given by $I = V_O/R_L$, where V_O is output voltage across the load resistance R_L.

From the following relation the sensor resistance R_S has been determined:

$$V_I = I(R_S + R_L), \quad (2)$$

where R_S is the sensor resistance and R_L is the load resistance, respectively.

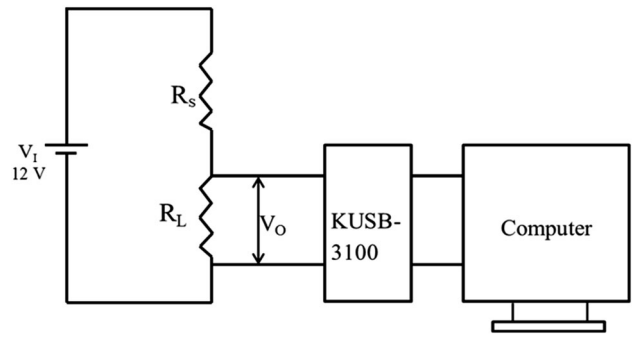

Fig. 1. The schematics of circuit diagram for data acquisition system.

In order to evaluate intergranular activation energy, the conductance of samples at different temperatures has been measured using the following relation:

$$G = 1/R_S. \quad (3)$$

RESULTS AND DISCUSSION

X-Ray Diffraction

For studying structural properties, an x-ray diffraction (XRD) pattern of all the samples has been recorded, which is shown in Fig. 2. The diffraction peaks of undoped as well as Ga-doped SnO_2 nanoparticles were compared with standard JCPDS data (file no. 41-1445) which revealed tetragonal rutile structure. Furthermore, the XRD pattern of doped nanoparticles did not show a peak pertaining to gallium or its oxide which revealed successful entry of Ga into the SnO_2 lattice. The intensity of diffraction peaks was found to be reduced with an increase in Ga content which is attributed to the formation of a large number of defects in doped SnO_2.[29] It has been found that the width of XRD peaks increases with increase in Ga content which indicated reduction in crystallite size of Ga doped nanoparticles. The crystallite size of all the samples has been evaluated using Scherrer's formula.[30] The average crystallite size of undoped and Ga-doped SnO_2 samples has been calculated using (110), (101), (200), (211) and (220) diffraction peaks, which is displayed in Table I. The decrease in size of SnO_2 with increase in dopant concentration is attributed to formation of a large number of nucleation centers formed just at the time of nanoparticle synthesis.

BET Study

Table I displays BET results of a surface area of undoped and Ga-doped SnO_2 nanoparticles. It is

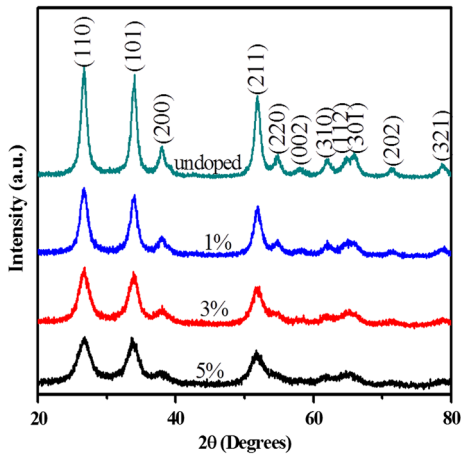

Fig. 2. XRD pattern of undoped and Ga-doped SnO_2 nanoparticles.

Table I. Crystallite size and surface area of undoped and Ga-doped SnO_2 nanoparticles

Sample	Crystallite size from XRD (nm)	Particle size from TEM (nm)	BET surface area (m^2/g)
Undoped	10.79	11	35
1%	8.5	–	40
3%	6	7	52
5%	5.6	–	54

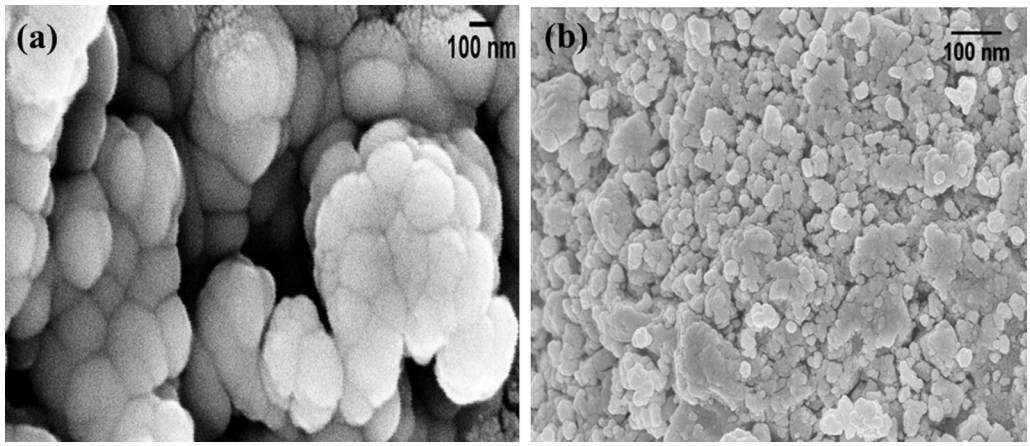

Fig. 3. FESEM images of (a) undoped and (b) 3% Ga-doped SnO_2 nanoparticles.

found that the BET surface area increases systematically with the rise in Ga content. The above results well agree with XRD results.

Field Emission Scanning Electron Microscopy

In order to investigate surface morphology, FESEM images (Fig. 3a and b) of undoped and 3% Ga-doped SnO_2 nanoparticles have been recorded. Undoped as well as Ga-doped SnO_2 samples exhibited almost spherical morphology. It is obvious from Fig. 3 that Ga-doping considerably reduced the grain size of SnO_2 nanoparticles. These results are well matched with XRD and BET study.

Transmission Electron Microscopy

To investigate morphology and crystal structure, we have recorded TEM and HRTEM images of undoped and Ga-doped SnO_2 nanoparticles. TEM images of undoped as well as 3% Ga-doped SnO_2 nanoparticles are shown in Fig. 4a and b. It has been observed that doping reduces (Table I) the particle size of SnO_2 samples. These results are in good agreement with XRD and BET investigations. HRTEM image (Fig. 4c) of 3% Ga-doped SnO_2 nanoparticles demonstrated well-defined atomic planes. The calculated value of interplanar spacing for 3% Ga-doped SnO_2 of nanoparticles is found to be equal to 0.33 nm which matches well with the (110) plane of tetragonal rutile SnO_2.

X-Ray Photoelectron Spectroscopy

In order to confirm the chemical oxidation states of elements present, XPS measurements were carried out on Ga-doped SnO_2 nanoparticles. Figure 5 displays high resolution XPS spectra of Sn 3d, O 1*s* and Ga 2p for 3% Ga-doped SnO_2 nanoparticles. The Sn 3d spectrum (Fig. 5a) exhibited two symmetric peaks $Sn3d_{3/2}$ and $Sn3d_{5/2}$ located at 484.36 eV and 492.77 eV, respectively, having a binding energy difference of 8.41 eV.[31] The presence of the above peaks in the Sn 3d spectrum confirmed the + 4 oxidation state of Sn in Ga-doped SnO_2 nanoparticles. The O1*s* spectra (Fig. 5b) represents an asymmetric peak, deconvolution of which gives two peaks positioned at 528.19 eV and 529.6 eV, respectively.[31,32] The peak positioned at 528.19 eV is ascribed to crystal lattice oxygen in Ga-doped SnO_2. On the other hand, the peak located at 529.6 eV corresponds to surface oxygen vacancies in Ga-doped SnO_2. It is a well-known fact that surface oxygen vacancies play an important role in gas sensing mechanisms. The high resolution spectrum of Ga 2p (Fig. 5c) displays two peaks Ga 2p3/2, and Ga 2p1/2 positioned at 1116.1 eV and 1142.7 eV, respectively, which indicate presence of Ga^{3+} in Ga-doped SnO_2.[33] The above results suggest the presence of Ga^{3+} in Ga-doped SnO_2.

Raman Spectroscopy

In order to examine the effect of Ga-doping on surface defects such as oxygen vacancies, room

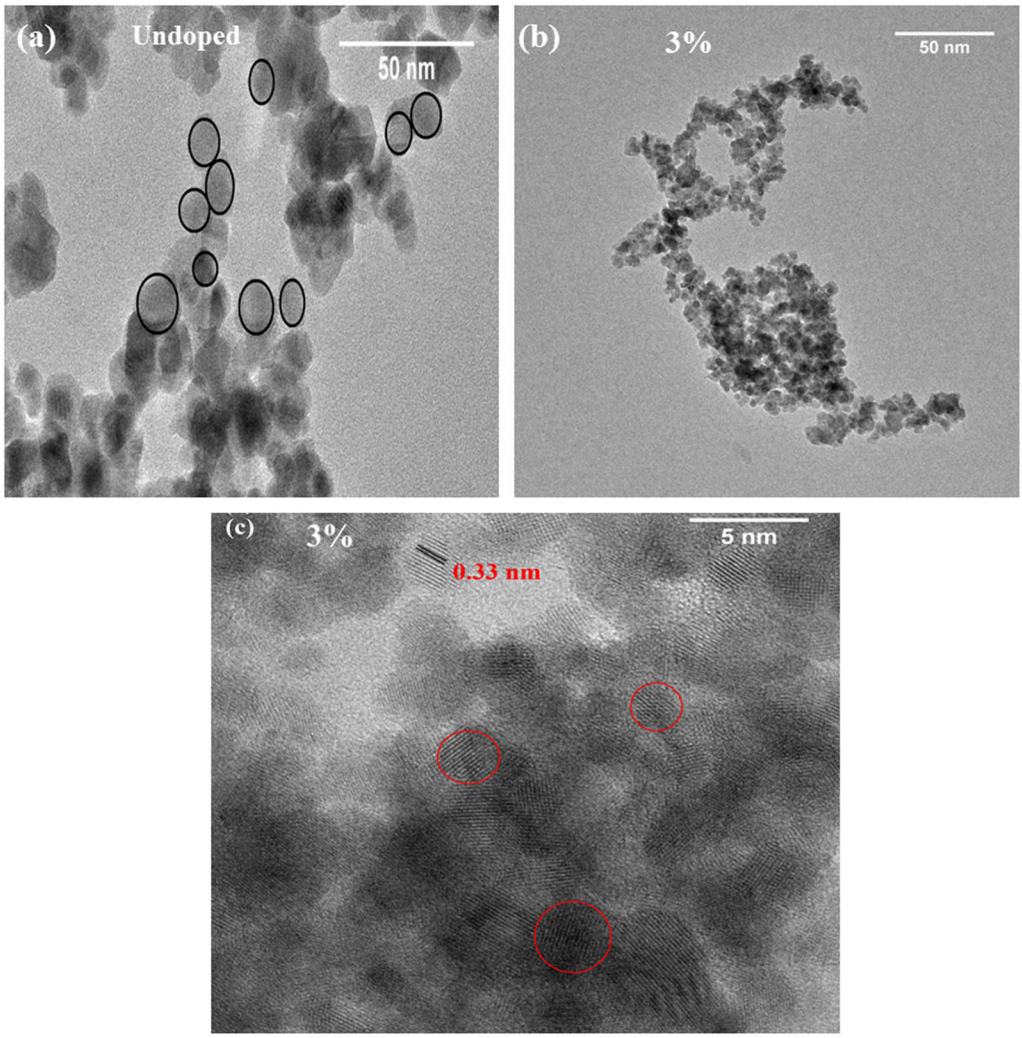

Fig. 4. TEM images of (a) undoped and (b) 3% Ga-doped SnO_2 nanoparticles, (c) HRTEM image of 3% Ga-doped SnO_2 nanoparticles.

temperature Raman spectra of all samples have been recorded. Figure 6a displays the Raman spectra of fabricated nanoparticles at an excitation wavelength of 514 nm. All the samples show peaks at 475 cm^{-1}, 632 cm^{-1} and 775 cm^{-1} which are related to E_g, A_{1g} and B_{2g} vibrations of SnO_2 respectively. These bands are fingerprints of tetragonal rutile structure of SnO_2.[34] The expansion and contraction of Sn-O bonds cause A_{1g} and B_{2g} bands to appear in Raman spectra.[35] The surface reconstruction of a (110) surface of SnO_2 gives up to three monolayers of atoms having oxygen vacancies at three different positions. There exist different types of oxygen vacancies in SnO_2 such as in-plane oxygen vacancies, bridging oxygen vacancies and sub-bridging oxygen vacancies. According to the literature A_{1g} mode is linked with bridging oxygen vacancies in a (110) SnO_2 surface.[36] It has been found that an A_{1g} band moves (Fig. 6b) towards lower wavenumber with increase in Ga content. Liu et al.[36] observed that an A_{1g} mode moves towards a lower wave number with increase in concentration of bridging oxygen vacancies of SnO_2. Therefore, in the present study shifting in the position of A_{1g} mode with rise in Ga concentration is ascribed to increase in concentration of bridging oxygen vacancies. Moreover, it has been found that shifting of A_{1g} towards lower wave number is attributed to the phonon confinement effect.[37] At nanoscale, the wave function of phonon no longer remains a plane wave and localization of wave function causes break down of the $k = 0$ selection rule. Therefore, phonons with wave vector $k = 0$ as well as $k > 0$ participate in Raman scattering which leads to shifting and broadening of A_{1g} band with increase in dopant concentration. It is reported that in-plane oxygen vacancies are related to the shallow donor states whereas bridging oxygen vacancies are linked with deeper states.[38] Interestingly, Raman spectra of all the samples display a broad band in the wavenumber range of 390–607 cm^{-1} and fitting of which (Fig. 6c) gives two extra bands located at 493 (S_1) cm^{-1} and 563 (S_2) cm^{-1} called Raman surface modes. These bands appear due to a small sized

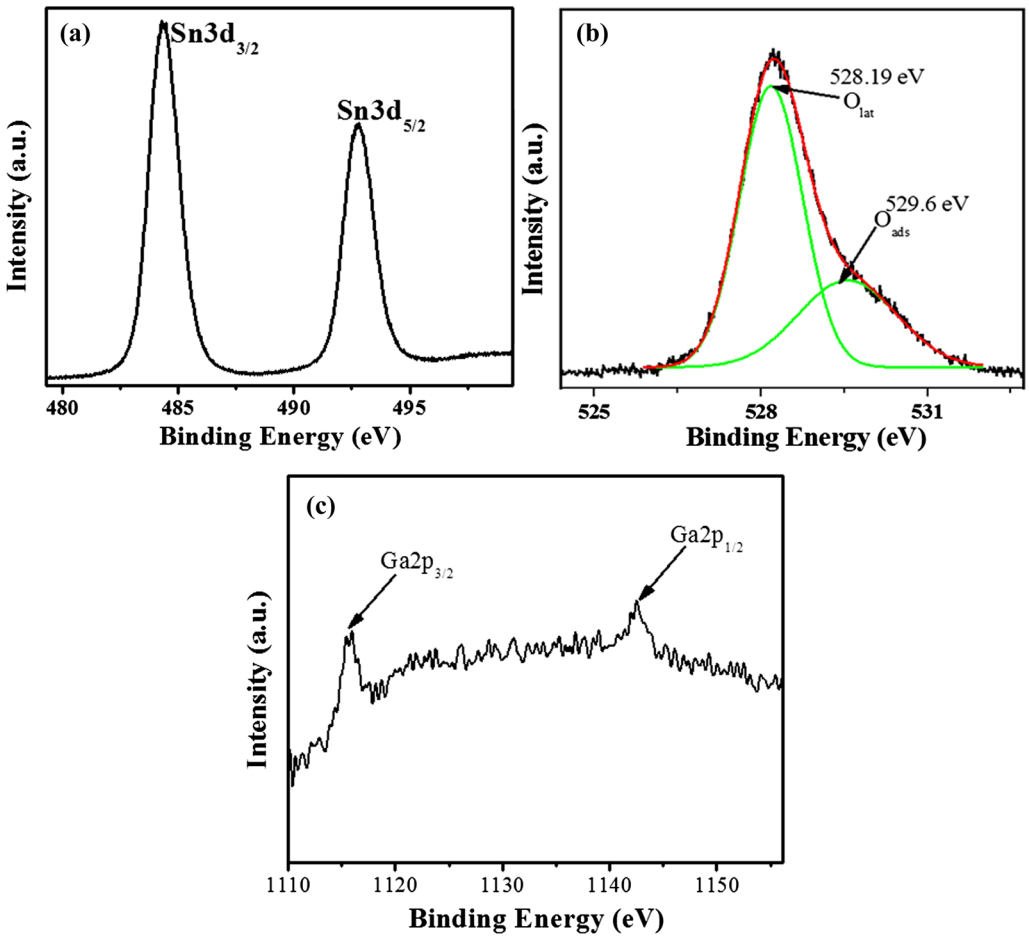

Fig. 5. High resolution XPS spectra of (a) Sn3d, (b) O 1*s* and (c) Ga 2p.

effect as explained by the Matossi force constant model.[39] Moreover, bands S_1 and S_2 do not appear in Raman spectra of bulk SnO_2 but are generally observed in nanostructured SnO_2. The surface disorder is likely to increase in nanostructured material consequently some forbidden modes become Raman active. It has been reported that the $k = 0$ selection rule gets relaxed in nanostructured materials due to the presence of a large number of surface defects (oxygen vacancies) and, as a result, some forbidden modes appear in Raman spectra of SnO_2.[40] The fitted Raman spectra of 3% Ga-doped SnO_2 are shown in Fig. 6c. Liu et al. reported that bands S_1 and S_2 are linked with in-plane oxygen vacancies at the surface of SnO_2 and the augmentation in intensity of these bands is attributed to the increment of in plane oxygen vacancies.[41] In order to investigate the effect of Ga-doping on the in-plane oxygen vacancies of SnO_2 we have taken the intensity ratio of surface modes (I_{S1+S2}) to A_{1g} mode (I_{A1g}) which is presented in Fig. 6d, where I_{S1+S2} is the sum of intensities of modes S_1 and S_2 and I_{A1g} is the intensity of A_{1g} mode. It is clear from Fig. 6d that the concentration of in-plane oxygen vacancies increases with rise in Ga content. The increase in concentration of in-plane oxygen vacancies with rise in Ga concentration suggest that Sn^{4+} is successfully replaced by Ga^{3+} ions in the SnO_2 lattice. Moreover, a peak positioned at 310 cm^{-1} has been detected which only appears in nanostructured materials.[42] Raman data indicated that Ga-doped SnO_2 nanoparticles containing abundant in-plane oxygen vacancies along with bridging oxygen vacancies.

Photoluminescence Spectroscopy

Photoluminescence Spectroscopy is an excellent technique that gives an idea about types of oxygen vacancies present in nanomaterials. The replacement of Sn^{4+} ions by Ga^{3+} ions leads to production of oxygen vacancies in a SnO_2 lattice owing to charge balance obligation. In SnO_2 oxygen vacancies are found to be foremost defects which are also known as irradiative centers.[43] The oxygen vacancies in SnO_2 occur in various states, for example, in neutral oxygen vacancies, singly charged oxygen and doubly charged oxygen vacancies.[44] Room temperature PL emission spectra of undoped and Ga-doped SnO_2 samples shown in Fig. 7 have been registered at an excitation wavelength of 300 nm. According to the literature, PL emission spectra of SnO_2 generally

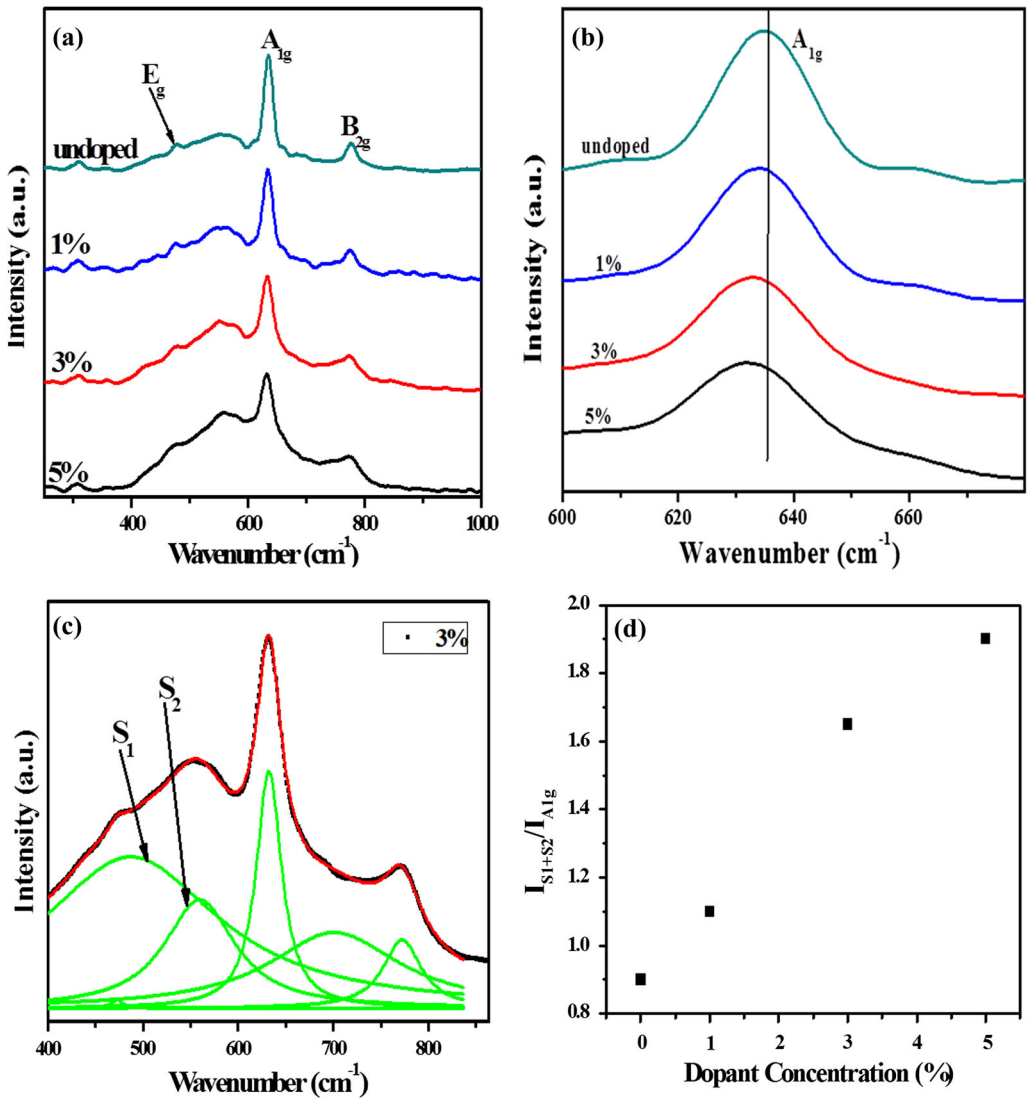

Fig. 6. (a) Raman spectra of undoped and Ga-doped SnO_2 nanoparticles, (b) shifting of A_{1g} band as a function of dopant concentration, (c) Fitted Raman spectra of 3% Ga-doped SnO_2 nanoparticles, (d) variation of $(I_{S1+S2})/(I_{A1g})$ ratio as a function of dopant concentration.

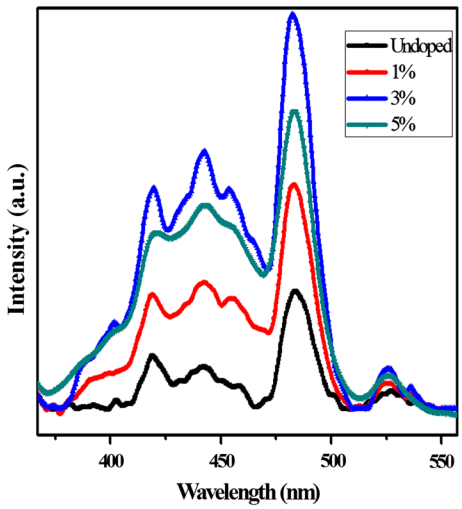

Fig. 7. PL spectra of undoped and Ga-doped SnO_2 nanoparticles.

display peaks corresponding to defects such as tin interstitials, oxygen vacancies and dangling bonds.[45] It has been observed that PL emission spectra of all the samples show peaks at 419 nm, 441 nm, 453 nm, 484 nm, 525 nm, respectively. It is found from the literature that PL emission peaks in the region 350–580 nm are attributed to the deep or shallow energy levels of oxygen vacancies.[46,47] Therefore, we claim that observed emission peaks are related to the defect energy levels of oxygen vacancies or tin interstitials of SnO_2. Jean et al.[48] reported that the emission peak located at around 484 nm is related to in-plane oxygen vacancies of SnO_2. Therefore, we suggest that the observed emission peak situated at 484 nm appears due to in-plane oxygen vacancies of SnO_2. These results are in good agreement with the Raman results. The enhancement in intensity (Fig. 7) of emission peaks has been seen with a rise in dopant concentration

which is attributed to increase in defect concentration.

GAS SENSING PROPERTIES

Gas Sensor Response

It is a well known fact that gas sensing properties of SnO_2 based sensors are deeply influenced by the operating temperature and dopant concentration. Therefore, it is necessary to investigate the optimum operating temperature of fabricated sensors. For that, sensor response (towards acetone and hydrogen) of fabricated sensors has been recorded at different operating temperatures. Figure 8a and b shows sensor response of undoped and Ga-doped sensors to 100 ppm of acetone and hydrogen at different operating temperatures. It is obvious from Fig. 8a and b that sensor response towards acetone and hydrogen increases, optimizes, and finally drops with rise in operating temperature. The gas sensing mechanism of a SnO_2 based sensor is based on reaction kinetics between surface adsorbed oxygen and test gas molecules. At a lower operating temperature target gas molecules cannot react with adsorbed oxygen and as a consequent the sensor displays negligible sensor response. With increased operating temperature, most of target gas molecules at the surface get sufficient energy to overcome an activation energy barrier in order to react with adsorbed oxygen and, as a result, sensor response increases.[49] Desorption of chemisorbed oxygen at higher operating temperature causes weakening of sensor response. The optimum operating temperature of an undoped sensor for acetone and hydrogen has been observed at 200°C and 350°C, respectively. The difference in optimum operating temperatures is attributed to different bond dissociation energies of acetone and hydrogen.[50] Acetone has a relatively lower bond dissociation energy (393 kJ/mol), as a result, it could easily react catalytically with adsorbed oxygen at lower operating temperatures. Consequently, optimum response towards acetone has been obtained at relatively lower operating temperature, i.e., 200°C. On the other hand, hydrogen is more inert because of its higher bond dissociation energy (436 kJ/mol) and, as a result, more energy is required for hydrogen to catalytically react with adsorbed oxygen. Therefore, the optimum operating temperature for hydrogen has been observed at a higher operating temperature.

It can be seen from Fig. 8b that optimum operating temperature of Ga-doped SnO_2 sensor for hydrogen is reduced to 300°C. The reduction in optimum operating temperature towards hydrogen is attributed to change in energy barrier height due to doping of Ga into SnO_2. The above observations indicate that addition of Ga into SnO_2 lead to decrease in optimum operating temperature of SnO_2 based sensor towards hydrogen. Furthermore, it has been revealed that a 3% Ga-doped SnO_2 based sensor displays an exceptionally large response towards acetone and hydrogen as compared to undoped and other doped sensors.

Response-recovery time is also a key parameter fora high performance gas sensor. The response time is defined as time required for the response to reach 90% of the equilibrium value after gas is introduced into a test chamber whereas recovery time is the time necessary for the sensor to reach a response 10% above its original value in air ambience. The response and recovery times of a metal oxide based gas sensor are directly related to the chemisorption and desorption process of gas on the surface of a sensor, respectively. Figure 9a and b represent response-recovery characteristic graphs of undoped and Ga-doped SnO_2 sensor towards 100 ppm of acetone and hydrogen at 200°C and 300°C, respectively. Evidently, sensor response towards acetone and hydrogen increases up to 3% dopant concentration whereas it decreases with

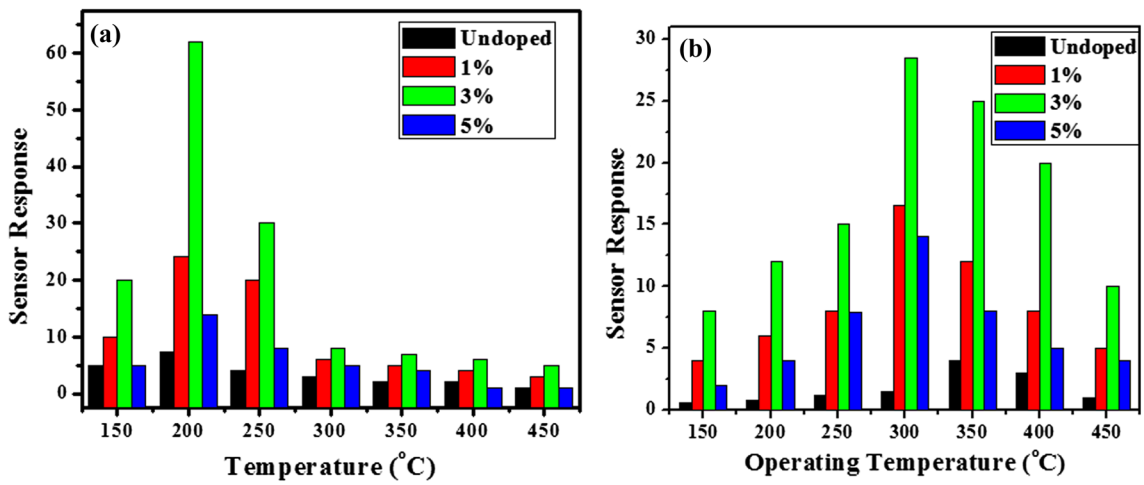

Fig. 8. sensor response of undoped and Ga-doped SnO_2 sensors towards 100 ppm of (a) acetone and (b) hydrogen at different operating temperature.

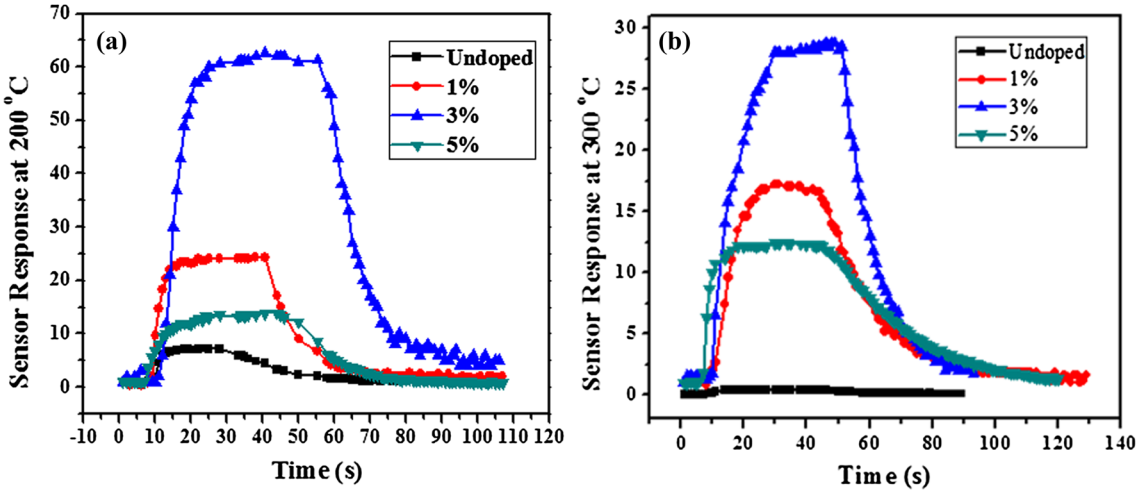

Fig. 9. Response-recovery characteristic graph of undoped and Ga-doped SnO_2 sensors towards (a) 100 ppm of acetone at 200°C and (b) 100 ppm of hydrogen at 300°C, respectively.

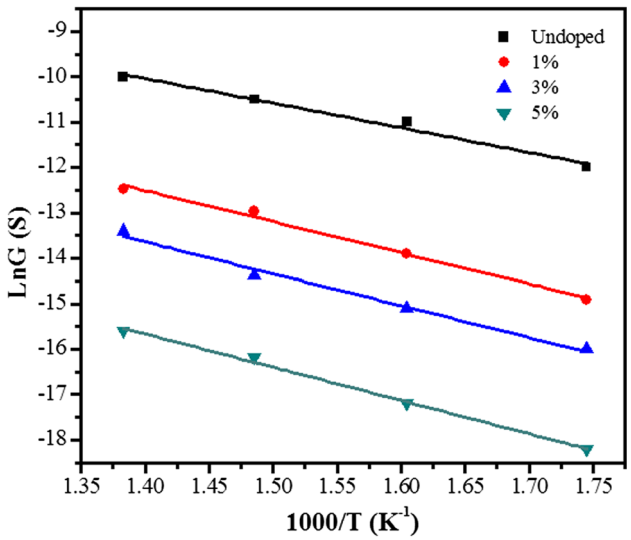

Fig. 10. Temperature dependence of conductance of SnO_2 and Ga-doped SnO_2 sensors.

further increase in dopant concentration. The calculated value of response and recovery time of 3% Ga-doped SnO_2 sensor towards 100 ppm acetone at 200°C is found to be 11 s and 43 s, whereas for hydrogen it is 20 s and 48 s, respectively. The fast response and recovery time of 3% Ga-doped SnO_2-based sensor towards acetone and hydrogen make it perfect for commercial applications.

Electrical Properties

The height of the energy barrier between the adjacent grains (known as activation energy) is a notable parameter which greatly influences the gas sensing properties of SnO_2 based sensors. The activation energy of all the samples has been calculated by using the following relation:[51]

Table II. Intergranular activation energy of undoped and Ga-doped SnO_2 samples

Sample	Activation energy (eV)
Undoped	0.466
1%	0.58
3%	0.60
5%	0.63

$$G = G_o \exp((-eV_S/kT)), \quad (4)$$

where G_o is the factor that comprises bulk intergranular conductance, k is the Boltzmann's constant, T is the absolute temperature, eV_S represents the potential energy barrier at the interface of two adjacent grains. The activation energy of undoped and Ga-doped SnO_2 samples has been determined from the plot of $1000/T$ versus ln G, where conductance G is in Siemens (S). The slope of plot (Fig. 10) gives the value of activation energy and calculated values of activation energy for undoped and Ga-doped SnO_2 sensors are listed in Table II. It is obvious from Table II that activation energy or intergranular energy barrier increases with decrease in size which is in accordance with the model reported by Rothschild and Komem.[13] This model states that as the grain size decreases the thickness of depletion layer, (L) increases whereas the conducting region shrinks leading to increase of activation energy barrier.

Gas Sensing Mechanism

The gas sensing mechanism of SnO_2 based sensors is based on a variation of resistance caused by adsorption and desorption of oxygen species. When a SnO_2 based sensor is placed in air ambience, the oxygen molecules from the atmosphere are adsorbed on its surface which withdraw electrons from the

conduction band of SnO_2 to form O_2^-, O^- and O^{2-} on the surface of SnO_2.[52,53] This process induces an electron depletion layer (space charge layer) on the surface of SnO_2. Moreover, the electron depletion layer on the surface of grains generates a potential barrier between the neighboring grains and, as a consequence, resistance of SnO_2 increases significantly. The potential barriers act as resistors and total resistance of SnO_2 is equal to the sum of grain boundary resistance. The electron must cross the electron depletion layer and the potential barrier for producing current. The reaction kinetics can be represented as follows:

$$O_2(\text{air}) \leftrightarrow O_2(\text{ads}), \tag{5}$$

$$O_2(\text{ads}) + e^- \leftrightarrow O_2^-(\text{ads}), \tag{6}$$

$$O_2^-(\text{ads}) + e^- \leftrightarrow 2O^-(\text{ads}), \tag{7}$$

$$O^-(\text{ads}) + e^- \leftrightarrow O^{2-}(\text{ads}). \tag{8}$$

Mishra et al.[54] investigated the effect of temperature on the different oxygen species. They found that below 160°C O_2^- dominates on the SnO_2 surface, whereas above 160°C O^- rules on the SnO_2 surface. When a SnO_2 based sensor is exposed to reducing gases such as hydrogen and acetone, a chemical interaction takes place between adsorbed oxygen and target gases (acetone and hydrogen) and, as a result, a captured electron is released back to the conduction band of sensing material. This process decreases the thickness of the depletion layer and the height of the potential barrier and, as a result, resistance of a SnO_2 based sensor decreases.[53]

The reaction between adsorbed oxygen and reducing gases (acetone and hydrogen) can be represented as:

$$CH_3COCH_3(\text{gas}) + 8O^- \rightarrow 3CO_2(\text{gas}) + 3H_2O + 8e^-, \tag{9}$$

$$H_2 + O^- \rightarrow H_2O + e^-. \tag{10}$$

Discussion

As discussed above Ga-doping significantly improved the sensor response of SnO_2 towards acetone and hydrogen. The sensor response is highly dependent on the amount of adsorbed oxygen on the surface of sensing material.[55] Augmented amounts of adsorbed oxygen species on the surface of sensing material can make contact with an enormous number of target gas molecules resulting in a large variation in resistance and hence response.

The plausible reason for enhanced sensor response of Ga-doped samples has been investigated and is discussed below:

(1) It is a well known fact that sensor response increases with increase in specific surface area of sensing material. It is already confirmed from BET study (Table I) that 3% Ga-doped SnO_2 nanoparticles possess a larger surface area as compared to undoped nanoparticles. It is a well known fact that material possessing a larger surface area exhibits higher response to various gases. The increased surface area of 3% Ga-doped SnO_2 nanoparticles helps in adsorbing more oxygen to interact with the target gases which results in enhanced sensor response.[56]

(2) PL and Raman spectroscopy demonstrated that concentration of oxygen vacancies increases with increase in Ga content. The oxygen vacancies in SnO_2 are created owing to substitution of Sn^{4+} ions by Ga^{3+} ions. Several researchers reported that oxygen vacancies boost the adsorption of oxygen species at the surface of the metal oxide.[57,58] It has been revealed that 3% Ga-doped SnO_2 based sensor exhibited higher resistance (in air ambience) as compared to undoped SnO_2 based sensor. The calculated value of resistance at 200°C and 300°C was found to be 0.5 and 0.2 MΩ for undoped sensor and 60 and 20 MΩ for 3% Ga-doped $SnO_{,2}$ respectively. This significant increase in resistance of 3% Ga-doped SnO_2 based sensor in air ambience is ascribed to increased concentration of adsorbed oxygen on its surface. The augmented amount of oxygen vacancies in 3% Ga-doped SnO_2 facilitates the adsorption of ambient oxygen on the Ga-doped SnO_2 surface which ultimately enlarges the potential barrier and width of space charge layer, hence increasing resistance of 3% Ga-doped SnO_2. Moreover, an increased ammount of adsorbed oxygen can make contact with the target gases resulting in large variation in electrical resistance, hence response. Therefore, it can be concluded that sensor response of SnO_2 based sensors increases with increase in concentration of oxygen vacancies.

(3) It is a well known fact that the thickness of space charge layer or electron depletion layer is generally related to Debye length of electrons. The Debye length $_D$ can be defined as:[59]

$$\lambda_D = \left(\frac{\varepsilon k_B T}{q^2 n_c}\right)^{1/2}. \tag{11}$$

where, ε represents the static dielectric constant $(9.0 \times 8.85 \times 10^{-12}\ \text{F m}^{-1})$ of SnO_2, k_B is the Boltzmann's constant (/

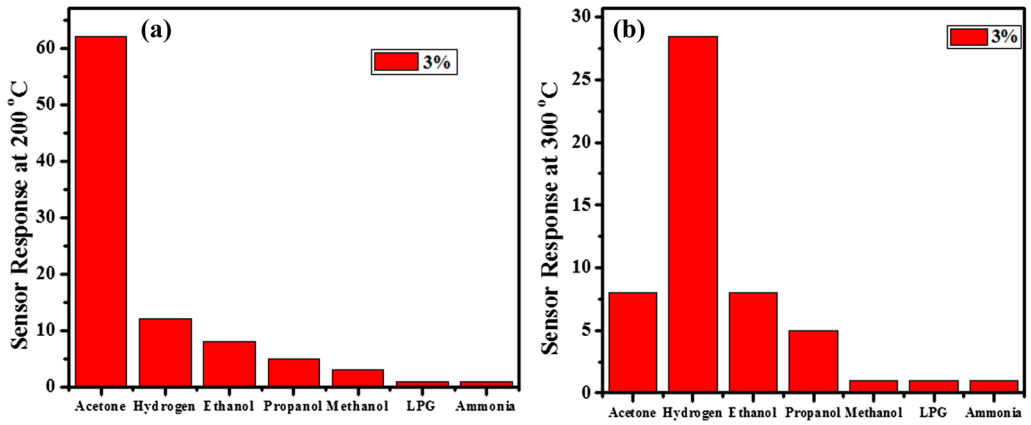

Fig. 11. (a) sensor response of 3% Ga-doped SnO_2 sensor towards 100 ppm of different gases at 200°C, (b) sensor response of 3% Ga-doped SnO_2 sensor towards 100 ppm of different gases at 300°C.

1.38×10^{-38} J K^{-1}), q is the electrical charge (1.6×10^{-19} C) of carrier. T is the absolute temperature (300 K) whereas n_c is the carrier concentration of SnO_2. The carrier concentration of SnO_2 at 300 K is found to be 3.6×10^{18} cm^{-3}. The calculated value of Debye length is found to be 3.2 nm. If the diameter of SnO_2 is nearly equal to twice the Debye length, then grains of SnO_2 are almost completely depleted. In our work, average particle size of 3% Ga-doped SnO_2 (6 nm) is comparable to twice the Debye length. Therefore, the amount of adsorbed oxygen on the surface of 3% Ga-doped SnO_2 is optimum to make maximum contact with the target gas molecule resulting in large variation in resistance. Hence, a 3% Ga doped SnO_2 based sensor exhibited enhanced response towards hydrogen and acetone.

(4) Moreover, abundant in-plane oxygen vacancies (confirmed from Raman and PL) of 3% Ga-doped SnO_2 samples facilitated the detection of acetone at a low temperature, i.e., 200°C.[22]

Temperature Dependent Selectivity

Selectivity of a sensor is one of the most important parameters to be considered for the commercialization of a gas sensor. For determining temperature dependent selectivity of 3% Ga-doped SnO_2 sensor, it was tested with 100 ppm of various gases at 200°C and 300°C, respectively. Figure 11a and b represents sensor response of 3% Ga-doped SnO_2 sensor towards 100 ppm of acetone, hydrogen, ethanol, methanol, ammonia and LPG at 200°C and 300°C, respectively. It has been observed that 3% Ga-doped SnO_2 sensor exhibits temperature dependent selectivity towards acetone and hydrogen. It is clear from Fig. 11a and b that 3% Ga-doped SnO_2 sensor is selective to acetone at 200°C, whereas it is selective to hydrogen at 300°C. It has been reported that compounds having oxygen atoms such as acetone can be easily adsorbed and interact with surface adsorbed oxygen of SnO_2. On the other hand, hydrogen being stable gas difficult to be adsorbed at low operating temperature on SnO_2. As a result, the optimum operating temperature of SnO_2 based sensor towards hydrogen has been observed at higher operating temperatures as compared to acetone.[20] Yoon et al.[60] reported selectivity of metal oxide based sensor towards various gases at different operating temperatures, their study revealed that selectivity of metal oxide sensors is linked with reaction activity of analyte gases to sensing material. Therefore, temperature dependent selectivity of a 3% Ga-doped SnO_2 based sensor towards acetone and hydrogen is attributed to different reaction activities of test gases. The selectivity of a sensor can be tuned by the adjusting of its operating temperature. The temperature dependent selectivity of a gas sensor is an important tool for detecting two or more gases simultaneously by adjusting the operating temperature of a gas sensor.

Repeatability

The repeatability of a 3% Ga-doped SnO_2 sensor towards 100 ppm of acetone and hydrogen at their optimum operating temperature has been evaluated by recording the sensor response four times successively as shown in Fig. 12a and b. Evidently, sensor retains its initial response even after four times of repetitive operation demonstrating excellent repeatability of the sensor.

Variation of Sensor Response as a Function of Acetone and Hydrogen Concentration

Figure 13a and b displays sensor response of 3% Ga-doped sensors as a function of acetone and hydrogen concentration at their optimum operating temperature, i.e., 200°C and 300°C, respectively. It has been observed that sensor response increases

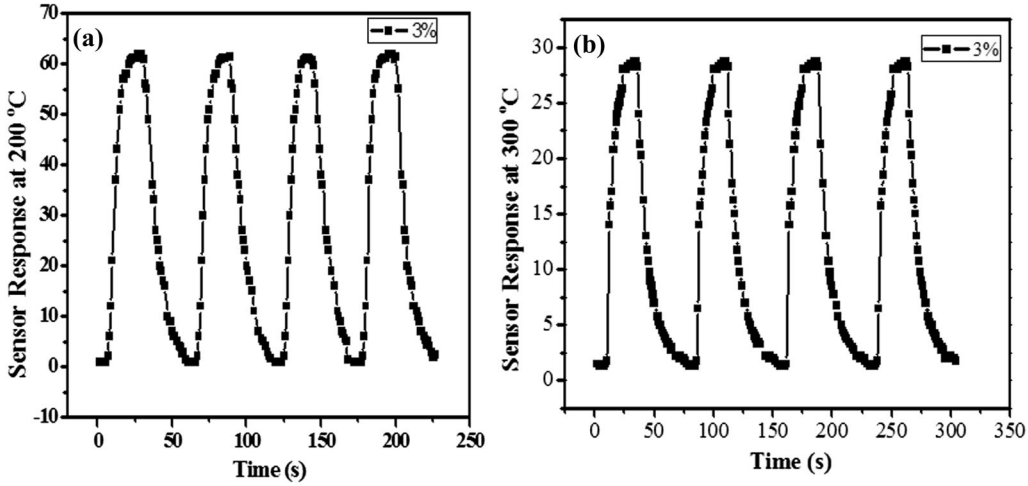

Fig. 12. (a) Repeatability of 3% Ga-doped sensor on successive exposure to 100 ppm of acetone at 200°C and (b) Repeatability of 3% Ga-doped SnO_2 sensor on successive exposure to 100 ppm of hydrogen at 300°C.

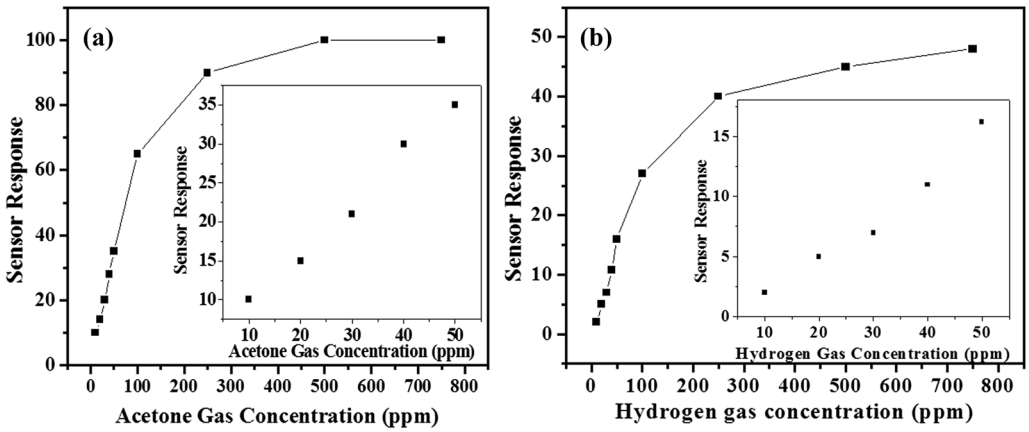

Fig. 13. (a) Variation of sensor response of 3% Ga-doped SnO_2 sensor as a function of acetone concentration at 200°C, (b) variation of sensor response of 3% Ga-doped SnO_2 sensor as a function of hydrogen gas concentration at 300°C.

linearly with increase in acetone and hydrogen gas concentration and saturates at higher concentration. Inset of figures shows the response of 3% Ga-doped SnO_2 at low concentration of acetone and hydrogen.

CONCLUSIONS

Ga-doped SnO_2 nanoparticles were successfully fabricated using the cost effective co-precipitation method. It has been observed crystallite size decreases with increase in dopant concentration. The XPS result confirmed the presence of Ga^{3+} in Ga-doped SnO_2 nanoparticles. Raman and PL studies indicated that concentration of oxygen vacancies increases with rise in Ga content. The present study showed that a 3% Ga-doped SnO_2 based sensor displayed enhanced sensor response and temperature dependent selectivity towards 100 ppm of acetone and hydrogen. The increased surface area and enhanced concentration of oxygen vacancies of 3% Ga-doped SnO_2 nanoparticles are responsible for enhanced sensor response towards acetone and hydrogen. Moreover, it is found that sensor response increases with increase in intergranular activation energy. The in-plane oxygen vacancies enabled the detection of acetone at a low temperature. Finally, we conclude that Ga-doped SnO_2 nanostructures can be used for fabricating high performance acetone and hydrogen gas sensors.

REFERENCES

1. Z. Jiang, R. Zhao, B. Sun, G. Nie, H. Ji, J. Lei, and C. Wang, *Ceram. Int.* 42, 15881 (2016).
2. X. Lian, Y. Li, X. Tong, Y. Zou, X. Liu, D. An, and Q. Wang, *Appl. Surf. Sci.* 407, 447 (2017).
3. G. Singh, N. Kohli, and R.C. Singh, *J. Mater. Sci. Mater. Electron.* 28, 2257 (2017).
4. R.K. Mishra, S.B. Upadhyay, A. Kushwaha, T.H. Kim, G. Murali, R. Verma, M. Srivastava, J. Singh, P.P. Sahay, and S.H. Lee, *Nanoscale* 7, 11971 (2015).
5. G. Singh and R.C. Singh, *Ceram. Int.* 43, 2350 (2017).

6. N.M. Shaalan, T. Yamazaki, and T. Kikuta, *Sens. Actuators B* 153, 11 (2011).
7. J. Du, R. Zhao, Y. Xie, and J. Li, *Appl. Surf. Sci.* 346, 256 (2015).
8. Z. Wang, T. Zhang, T. Han, T. Fei, S. Liu, and G. Lu, *Sens. Actuators B* 266, 812 (2018).
9. J.H. Kim, J.H. Lee, A. Mirzaei, H.W. Kim, and S.S. Kim, *Sens. Actuators B* 258, 204 (2018).
10. S. Majumdar, *Ceram. Int.* 41, 14350 (2015).
11. G. Singh, M. Kaur, B. Arora, and R.C. Singh, *J. Mater. Sci. Mater. Electron.* 29, 867 (2018).
12. S. Habibzadeh, A.A. Khodadadi, and Y. Mortazavi, *Sens. Actuators B* 144, 131 (2010).
13. A. Rothschild and Y. Komem, *J. Appl. Phys.* 95, 6374 (2004).
14. T. Kida, S. Fujiyama, K. Suematsu, M. Yuasa, Y.J. Kwon, H.G. Na, S.Y. Kang, M.S. Choi, J.H. Bang, T.W. Kim, A. Mirzaei, and H.W. Kim, *Sens. Actuators B* 239, 180 (2017).
15. K. Shimanoe, *J. Phys. Chem. C* 117, 17574 (2013).
16. X. Kou, N. Xie, F. Chen, T. Wang, L. Guo, C. Wang, Q. Wang, J. Ma, Y. Sun, H. Zhang, and G. Lu, *Sens. Actuators B* 256, 861 (2018).
17. W. Zeng, T. Liu, D. Liu, and E. Han, *Sens. Actuators B* 160, 455 (2011).
18. G. Singh, N. Kohli, and R.C. Singh, *J. Mater. Sci. Mater. Electron.* 28, 13013 (2017).
19. X. Xu, M. Yin, N. Li, W. Wang, B. Sun, M. Liu, D. Zhang, Z. Li, and C. Wang, *Talanta* 167, 638 (2017).
20. Z. Lin, N. Li, Z. Chen, and P. Fu, *Sens. Actuators B* 239, 501 (2017).
21. P. Baraneedharan, S.I. Hussain, V.P. Dinesh, C. Siva, P. Biji, and M. Sivakumar, *Appl. Surf. Sci.* 357, 1511 (2015).
22. V. Bonu, A. Das, A.K. Prasad, N.G. Krishna, S. Dhara, and A.K. Tyagi, *Appl. Phys. Lett.* 105, 243102 (2014).
23. Y. Shen, T. Yamazaki, Z. Liu, D. Meng, T. Kikuta, N. Nakatani, M. Saito, and M. Mori, *Sens. Actuators B* 135, 524 (2009).
24. Y. Shen, T. Yamazaki, Z. Liu, D. Meng, and T. Kikuta, *J. Alloys Compd.* 488, L21 (2009).
25. X. Xie, Z. Shao, Q. Yang, X. Shen, W. Zhu, X. Hong, and G. Wang, *J. Solid State Chem.* 191, 46 (2012).
26. M. Hjiri, R. Dhahri, L. El Mir, A. Bonavita, N. Donato, S.G. Leonardi, and G. Neri, *J. Alloys Compd.* 634, 187 (2015).
27. C.Y. Tsay and S.C. Liang, *J. Alloys Compd.* 622, 644 (2015).
28. G. Singh, R. Thangaraj, and R.C. Singh, *Ceram. Int.* 42, 4323 (2016).
29. N. Lavanya, C. Sekar, E. Fazio, F. Neri, S.G. Leonardi, and G. Neri, *Int. J. Hydrogen Energy* 42, 10645 (2017).
30. A.L. Patterson, *Phys. Rev.* 56, 978 (1939).
31. G. Wang, Y. Yang, Q. Mu, and Y. Wang, *J. Alloys Compd.* 498, 81 (2010).
32. F.H. Arago, I. Gonzalez, J.A.H. Coaquira, P. Hidalgo, H.F. Brito, J.D. Ardisson, W.A.A. Macedo, and P.C. Morais, *J. Phys. Chem. C* 119, 8711 (2015).
33. L. Du, H. Li, S. Li, L. Liu, Y. Li, S. Xu, Y. Gong, Y. Cheng, X. Zeng, and Q. Liang, *Chem. Phys. Lett.* 713, 235 (2018).
34. P. Sangeetha, V. Sasirekha, and V. Ramakrishnan, *J. Raman Spectrosc.* 42, 1634 (2011).
35. P. Chetri, B. Saikia, and A. Choudhury, *J. Appl. Phys.* 113, 233514 (2013).
36. L.Z. Liu, T.H. Li, X.L. Wu, J.C. Shen, and P.K. Chu, *J. Raman Spectrosc.* 43, 1423 (2012).
37. J.P. Singh, R.C. Srivastava, H.M. Agrawal, and R. Kumar, *J. Raman Spectrosc.* 42, 1510 (2011).
38. L.Z. Liu, X.L. Wu, J.Q. Xu, T.H. Li, J.C. Shen, and P.K. Chu, *Appl. Phys. Lett.* 100, 121903 (2012).
39. Y.J. Chen, L. Nie, X.Y. Xue, Y.G. Wang, and T.H. Wang, *Appl. Phys. Lett.* 88, 083105 (2006).
40. W.B.H. Othmen, B. Sieber, H. Elhouichet, A. Addad, B. Gelloz, M. Moreau, S. Szunerits, and R. Boukherroub, *Mater. Sci. Semicond. Process.* 77, 31 (2018).
41. L.Z. Liu, X.L. Wu, F. Gao, J.C. Shen, T.H. Li, and P.K. Chu, *Solid State Commun.* 151, 811 (2011).
42. F.H. Aragon, J.A.H. Coaquira, P. Hidalgo, S.W. da Silva, S.L.M. Brito, D. Gouvea, and P.C. Morais, *J. Raman Spectrosc.* 42, 1081 (2011).
43. S. Deepa, K.P. Kumari, and B. Thomas, *Ceram. Int.* 43, 17128 (2017).
44. R.K. Mishra, S.K. Pandey, and P.P. Sahay, *Mater. Res. Bull.* 48, 4196 (2013).
45. S. Chacko, M.J. Bushiri, and V.K. Vaidyan, *J. Phys. D Appl. Phys.* 39, 4540 (2006).
46. S. Rani, S.C. Roy, N. Karar, and M.C. Bhatnagar, *Solid State Commun.* 141, 214 (2007).
47. A. Kar, S. Kundu, and A. Patra, *J. Phys. Chem. C* 115, 118 (2011).
48. S.-T. Jean and Y.C. Her, *J. Appl. Phys.* 105, 024310 (2009).
49. Y. Wang, C. Liu, L. Wang, J. Liu, B. Zhang, Y. Gao, P. Sun, Y. Sun, T. Zhang, and G. Lu, *Sens. Actuators B* 240, 1321 (2017).
50. C. Zhang, J. Wang, R. Hu, Q. Qiao, and X. Li, *Sens. Actuators B* 222, 1134 (2016).
51. A. Hastir, N. Kohli, O.S. Kang, and R.C. Singh, *J. Electroceram.* 37, 170 (2016).
52. T.T. Wang, S.Y. Ma, L. Cheng, J. Luo, X.H. Jiang, and W.X. Jin, *Sens. Actuators B* 216, 212 (2015).
53. Y. Chen, L. Yu, D. Feng, M. Zhuo, M. Zhang, E. Zhang, Z. Xu, Q. Li, and T. Wang, *Sens. Actuators B* 166–167, 61 (2012).
54. R.K. Mishra, A. Kushwaha, and P.P. Sahay, *RSC Adv.* 4, 3904 (2014).
55. Y. Guan, D. Wang, X. Zhou, P. Sun, H. Wang, J. Ma, and G. Lu, *Sens. Actuators B* 191, 45 (2014).
56. Y. Wang, Q. Mu, G. Wang, G. Wang, and Z. Zhou, *Sens. Actuators B* 145, 847 (2010).
57. S.A. Feyzabad, Y. Mortazavi, A.A. Khodadadi, and S. Hemmati, *Sens. Actuators B* 181, 910 (2013).
58. W.Q. Li, S.Y. Ma, Y.F. Li, X.B. Li, C.Y. Wang, X.H. Yang, L. Cheng, Y.Z. Mao, J. Luo, D.J. Gengzang, G.X. Wan, and X.L. Xu, *J. Alloys Compd.* 605, 80 (2014).
59. Y.J. Kwon, H.G. Na, S.Y. Kang, M.S. Choi, J.H. Bang, T.W. Kim, A. Mirzaei, and H.W. Kim, *Sens. Actuators B* 239, 180 (2017).
60. J.W. Yoon, H.J. Kim, I.D. Kim, and J.H. Lee, *Nanotechnology* 24, 8444005 (2013).